Colloids and Surfaces A: Physicochemical and Engineering Aspects 652 (2022) 129760

Contents lists available at ScienceDirect

Colloids and Surfaces A: Physicochemical and Engineering Aspects

journal homepage: www.elsevier.com/locate/colsurfa

Capping ligand initiated $CuInS_2$ quantum dots decoration on, $ZnIn_2S_4$ microspheres surface under different alkalinity levels resulting in different hydrogen evolution performance

Onur Cavdar [a], Anna Malankowska [a,*], Justyna Łuczak [b], Andrzej Żak [c], Wojciech Lisowski [d], Tomasz Klimczuk [e,f], Adriana Zaleska-Medynska [a]

[a] Department of Environmental Technology, Faculty of Chemistry, University of Gdansk, Gdansk, Poland
[b] Department of Process Engineering and Chemical Technology, Faculty of Chemistry, Gdansk University of Technology, Gdansk, Poland
[c] Electron Microscopy Laboratory, Faculty of Mechanical Engineering, Wroclaw University of Science and Technology, Gdansk, Poland
[d] Institute of Physical Chemistry, Polish Academy of Science, Warsaw, Poland
[e] Faculty of Applied Physics and Mathematics, Gdansk University of Technology, Narutowicza, Gdansk, Poland
[f] Advanced Materials Center, Gdansk University of Technology, Narutowicza, Gdansk, Poland

GRAPHICAL ABSTRACT

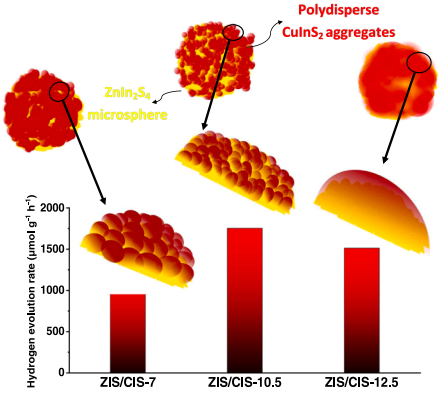

ARTICLE INFO

Keywords:
CuInS2
ZnIn2S4
Quantum dots
Visible light photoactivity
Hydrogen
Aggregates

ABSTRACT

Surface distribution of quantum dots (QDs) at the semiconductor matrix caused by synthesis condition (e.g. pH of solution during coupling) could lead to different photocatalytic activity. Thus, achieving an optimal covering of semiconductor matrix by QDs has been challenging. Herein, the influence of the alkalinity level of aqueous decoration medium for the coupling of mercaptoundecanoic acid (MUA) capped $CuInS_2$ quantum dots (CIS) and $ZnIn_2S_4$ microspheres (ZIS) on photocatalytic hydrogen evolution (PHE) performance was investigated. Aqueous decoration medium with different alkalinity levels for the formation of ZIS/CIS photocatalytic system resulted in significantly different PHE performances in the presence of (0.5 wt%) Pt co-catalyst deposition without any change in crystal structure of ZIS matrix up to pH 12.5. The photocatalytic system obtained at pH 10.5 possessed the highest performance followed by the decrease at pH 11.5 and again the remarkable increase was detected at

* Corresponding author.

https://doi.org/10.1016/j.colsurfa.2022.129760
Received 9 May 2022; Received in revised form 7 July 2022; Accepted 18 July 2022
Available online 20 July 2022

pH 12.5 that was the pH level for uniform dispersion of CIS in aqueous medium. This work remarks the importance of the nanoparticle's aggregates on PHE performance over non-toxic $ZnIn_2S_4/CuInS_2$ photocatalytic system.

1. Introduction

H_2 fuel has a great potential to reduce reliance on fossil fuels [1]. As one of one the solar conversion technology, photocatalytic water splitting has been drawing intensive attention to produce green H_2 [2]. For that purpose, metal sulfide based photocatalysts have been widely investigated due to relatively high conduction band edge that is thermodynamically suitable for H_2O reduction in the presence of sacrificial agents [3].

Among the various type of photocatalytic metal sulfide semiconductors [4–8], n-type $ZnIn_2S_4$ semiconductor based photocatalytic systems became prominent because $ZnIn_2S_4$ is easy to prepare, and has adjustable bandgap through doping and wide absorption range [9]. Several type of $ZnIn_2S_4$ based photocatalytic systems have been studied to overcome its low photocatalytic activity due to the rapid recombination of photogenerated charge carriers [10–16]. One of the other alternative method to induce the performance of $ZnIn_2S_4$ is to incorporate it with other metal sulfide-based nanomaterials such Ag_2S [17], Cu_2S [18], CdS [19], MoS_2 [20], WS_2 [21]. Besides, $ZnIn_2S_4/CuInS_2$ based photocatalytic system also have been attracted attention [22–24] owing to a large absorption coefficient of a typical p-type semiconductor $CuInS_2$ [25]. In our previous report, we obtained $ZnIn_2S_4$ microspheres (ZIS) decorated with pre-prepared $CuInS_2$ quantum dots (CIS QDs) capped with mercaptoundecanoic acid (MUA) by simply introducing CIS into ZIS precursors for hydrothermal treatment medium [26]. This approach resulted in significant increase in photocatalytic hydrogen evolution activity of pristine ZIS in the presence of Pt deposition. However, the formation of aggregates of CIS during the synthesis that resulted in an uneven distribution of CIS on ZIS surface. This has led to the question whether the different formation of those aggregates can affect the photocatalytic activity of ZIS/CIS photocatalytic system or not.

The pH dependent aggregation of mercaptocarboxylic acid capping ligand, such as thioglycolic acid and mercaptopropionic acid, capped quantum dots and its effect on their optoelectronic properties have been reported generally with the purpose of bioimaging applications [27–29]. Beyond the aggregation effect, Xu et al. reported that there are several reasons leading different optoelectronic properties of mercaptocarboxylic acid ligand capped quantum dots including thiol group effect, counter ions effect, and terminal group effect in which their contributions differ at different pH values [30]. However, to best of our knowledge, there are very limited reports on the effect of aggregation phenomenon on photocatalytic hydrogen evolution performance by controlling the decoration medium of mercaptocarboxylic acid ligand capped quantum dots on a surface of larger matrix. Yu et al. have studied the assembly of MPA-regulated CdSe QDs on commercial photocatalysis TiO_2 (P25) by adjusting the pH level of the interaction medium to alkaline level in order to avoid the aggregates of quantum dots in acidic conditions to be furtherly coupled with in-situ formed $Ni(OH)_2$ deposition [31]. On the other hand, PHE performances depending on the aggregation of single or double nanoparticle photocatalytic systems were investigated by several groups. For instance, Chang et al. reported that aggregates of CdS QDs were more favorable than that of CdS with aggregation preventing mercaptopropionic acid capping due to efficient charge separation with reduced charge carrier recombination [32] which was corroborative Park's work [33]. Moreover, Gao et al. suggested that the interparticle hole transfer which was accelerated by the formation of CdSe QDs-ZnSe QDs aggregation was the crucial factor for boosting the photocatalytic hydrogen evolution performance of the system [34]. Additionally, Sawaguchi-Sato et al. investigated the aggregation induced photocatalytic hydrogen evolution from Pt colloidal catalysts CdTe quantum dots photocatalytic system by means of the type of mercaptocarboxylic acid capping ligand on quantum dots surface that changed the formation of aggregation [35]. Considering above-referred works, aggregation can have an important role on photocatalytic hydrogen evolution.

In this study, we investigated the effect of the aggregation formation of mercaptoundecanoic acid capped (MUA) CIS by adjusting the alkalinity of aqueous decoration medium for the formation of ZIS/CIS photocatalytic system. Despite all obtained photocatalytic systems contained the same amount of CIS, the treatment of sample under different alkalinity levels resulted in significantly different photocatalytic hydrogen evolution performances in the presence of same amount of Pt cocatalyst under visible light irradiation. The possible reasons behind that were discussed in terms of information on the morphology, optoelectronic and surface chemistry properties.

2. Experimental

2.1. Materials

Cetyltrimethylammonium bromide (CTAB, 95 %) (Aldrich), indium (III) nitrate hydrate (99.99 %) (Alfa Aesar), thioacetamide (J.T. Baker, Avantar performance materials), copper (I) iodide (99.99 %) (Sigma-Aldrich), indium (III) acetate (99.99 %) (Acros Organics), thiourea (99.99 %) (CHEMPUR), 11-mercaptoundecanoic acid (95 %) (Sigma-Aldrich), zinc sulfate heptahydrate (99.99 %) (CHEMPUR), potassium tetrachloroplatinate (II), (99.9 %) (Alfa Aesar), methyl viologen dichloride hydrate (98 %) (Sigma-Aldrich). All chemicals were used without any further purification.

2.2. Synthesis of ZIS/CIS photocatalytic system

ZIS and CIS QDs were synthesized as mentioned in a previous report [26]. To obtain ZIS/CIS photocatalytic system, the ratio of CIS was fixed to 5 wt%. The pH level of aqueous medium (deionized water) for the decoration was adjusted to 7, 9.5, 10.5, 11.5, 12.5 and 12.9 by adding 0.1 M KOH or H_2SO_4 aqueous solution and the concentration of CIS quantum dots were always kept 2 mg/ml. After adding CIS to the aqueous decoration medium with desired pH level, the mixture was sonicated for 10 min and vigorously stirred for 30 min. Finally, ZIS powder was added, and all mixture was stirred for 24 h. The products were washed with ethanol and water and separated using centrifuge (6000 RPM) and dried at 60 °C. The products were abbreviated according to the pH level of aqueous decoration medium as ZIS/CIS-7, ZIS/CIS-9.5, ZIS/CIS-10.5, ZIS/CIS-11.5, ZIS/CIS-12.5 and ZIS/CIS-12.9. Samples during and after Pt in-situ deposition assisted PHE tests were abbreviated as ZIS/CIS-7/Pt, ZIS/CIS-9.5/Pt, ZIS/CIS-10.5/Pt, ZIS/CIS-11.5/Pt, ZIS/CIS-12.5/Pt and ZIS/CIS-12.9/Pt.

2.3. Characterization

To prove all the samples, have the same amount Pt or CIS, Pt and Cu content were analyzed by inductively coupled plasma optical emission spectroscopy (ICP-OES) using Agilent 5100 spectrometer, according to PN-EN ISO 11885:2009 standard. X-ray diffraction (XRD) technique was used to determine the crystalline structure of the samples and detect whether any changes has occurred in ZIS matrix during the preparation of ZIS/CIS samples. Powder X-ray diffraction experiments were

conducted at 20 °C on powdered samples with a Bruker D8 Focus diffractometer with Cu Kα (λ = 1.54 Å) radiation and a LynxEye XE-T detector. Data were collected from 5° to 70° 2θ over a scan time of 30 min. LeBail refinement of the pXRD pattern was performed to determine the crystal structure type of the tested samples, using High-Score Plus ver. 3.0e software. The chemical composition of samples surface (ZIS/CIS-7, ZIS/CIS-10.5 and ZIS-CIS-12.5) areas was analyzed by X-ray photoelectron spectroscopy (XPS) using a PHI 5000 VersaProbeTM spectrometer (ULVAC-PHI, Chigasaki, Japan) with monochromatic Al Kα irradiation (hν = 1486.6 eV) to highlight the reduction of Pt precursor over the samples during PHE leading to formation of Pt species. The high-resolution (HR) XPS spectra were recorded with the hemispherical analyzer at the pass energy of 23.5 eV and the energy step size of 0.1 eV. The morphology of samples (ZIS/CIS-7, ZIS/CIS-10.5 and ZIS-CIS-12.5) was observed using scanning electron microscope (SEM, JEOL JSM-7610F) and transmission electron microscope (TEM, Hitachi H-800 microscope, Hitachi High-Technologies) operating at 150 kV. The UV–vis spectra of samples were recorded using UV–vis spectrophotometer (Evolution 220, Thermo Scientific). The photoluminescence spectra (PL) were recorded using a PerkinElmer Luminescence Spectrometer LS-50B equipped with Xenon discharge lamp as an excitation source. The samples were excited with 330 nm at room temperature and the emission was scanned between 300 and 800 nm. Fourier-transform infrared spectroscopy (FTIR) (Bruker, IFS66) was used to identify the surface characteristics of CIS QDs and ZIS/CIS photocatalytic system in the scan range of 500–5000 cm^{-1} in the diffuse reflectance mode with a resolution of 0.12 cm^{-1} at room temperature and KBr was used as a reference material. Malvern Zetasizer Nano ZS or Mastersizer 3000 were used to measure CIS aggregates size under different alkalinity levels by dynamic light scattering (DLS) technique, the zeta potential of ZIS samples in the aqueous decoration medium and ZIS/CIS samples in photocatalytic hydrogen evolution reaction solution.

2.4. Photocatalytic hydrogen evolution experiments

50 mg photocatalyst was added into 50 ml 0.35 M Na_2S/0.25 M Na_2SO_3 aqueous solution in a beaker and the mixture was sonicated using ultrasonic bath for 5 min. The mixture was transferred to a photoreactor equipped with a quartz glass with 110 ml volume and 50 mM K_2PtCl_4 aqueous solution was dripped to deposit 0.5 wt% Pt on ZIS/CIS photocatalytic system's surface. After sealing the reactor with a plastic septum, the mixture was purged with N_2 gas with 12 dm^3/h flow rate for 30 min in dark. Finally, the mixture was irradiated by 1000 W Xenon lamp external light source (Quantum Design, LSH 602) equipped with a cut-off filter GG420 (Optel, λ > 420 nm). The temperature of the PHE process was always kept at 10 °C using a thermostat. The amount of hydrogen gas was monitored by adding 200 μl of gas sample collected from the headspace of the photoreactor within every using an air-tight syringe (Hamilton) to the gas chromatograph (Thermo Scientific TRACE 1300-GC, N_2 carrier) No hydrogen was evolved in the absence of ZIS/CIS photocatalyst under the same condition. The amount of hydrogen was calculated using calibration curve which was based on a collected data from GC-TCD and pressure value from a digital manometer (SIKA) attached to the photoreactor following addition of different volume of hydrogen (99.99 %) using an air-tight syringe (HAMILTON). Later, the amount of hydrogen in moles was calculated using the ideal gas equation [36]. The recycling performance tests were carried out under the same experimental conditions. After each cycle, the sample was collected and washed with deionized water by a centrifuge. The fresh 0.35 M Na_{2S}/0.25 M Na_2SO_3 aqueous solution was added in a centrifuge tube with the sample and then the mixture was poured into the photoreactor for the next cycle test. The pH of photocatalytic hydrogen evolution solution after one cycle was around 12.

3. Results and discussion

To reveal the different optical characteristics of CIS aggregates under different alkalinity levels, UV–vis and PL spectrum of samples was compared (Fig. 1). To conduct those measurements, the samples were dispersed in water with the pre-adjusted alkalinity level using 0.1 M H_2SO_4 or KOH solution and stirred vigorously following for 30 min following 10 min sonication. Particle concentration during all measurements was 0.5 mg/ml. From pH = 7 to pH = 11.5, the red-shifted absorption edge was observed that was followed by the drastic change in UV–vis spectra at pH = 12.5, and the specific absorption shoulder appeared at around 250 nm at pH = 12.5. Also, to check the spectrum only originating from MUA, MUA has been dispersed in aqueous solution with pH = 7, 10.5, and 12.5 and their absorbance spectra were recorded. The same peak at 250 nm can be observed from the absorption spectra only from MUA in pH 12.5 which has shown the spectrum with the similar trend as in MUA capped CIS (Fig. S1). However, considerable red-shifting was exhibited by MUA-capped CIS compared to that of only MUA. Likewise, the same red shifting is observed from the spectrum originating from MUA capped CIS under pH = 7 and 10.5 attributing to the coupling between the MUA and CIS [37]. Moreover, the aggregation induced emission was proven comparing the PL spectra of CIS aggregates under different alkalinity levels, as the emission intensity was the highest at pH = 7 and significantly dropped at pH = 11.5 and finally quenched at pH = 12.5 where the clear, red-colored dispersion of CIS were achieved (inset in Fig. 1b). The change in the optical properties of CIS aggregates which was mediated by alkalinity level can be explained by the degree of the aggregation considering the aggregation induced emission. To this respect, DLS was measured to show how the size of aggregates were distributed depending on the level of the alkalinity of aqueous medium. As seen from Fig. 2, all CIS aggregates displayed high polydispersity with macro-sized aggregates around 100 μm at pH = 9.5 and 10.5. At pH = 11.5, the aggregate size decreased noticeably along with the new peak formed corresponding 1 μm particle size. After reaching pH = 12, the size of aggregates was shifted to remarkably lower size and two significant peaks formed around 5 nm and 100 nm at pH = 12.5 and 12.9. The reason behind the macro-sized aggregation between the alkalinity level pH = 9.5–11.5 was due to the non-ionized carboxylic acid end group in MUA ligand on CIS surface [38–40]. Thus, inter-nanoparticle H-bonds through the hydrophilic groups on nanoparticle surface resulted in aggregation in a weak basic aqueous solution [38]. On the other hand, after high pH = 12, the carboxylic groups in MUA on CIS surface was deprotonated and stabilized CIS aggregates were achieved via electrostatic repulsion [41], so that the aggregation was reduced [42].

Accordingly, as the aggregate sizes of CIS under different alkalinity levels, it can be proposed that each CIS aggregates in aqueous medium under different alkalinity behaves different that led to different morphology of ZIS/CIS photocatalytic system. The SEM images (Fig. 3a–c) indicated that, at the pH = 12.5, ZIS microparticles surface were lesser overwhelmed by CIS and coating-like CIS on ZIS formed smooth surface on ZIS/CIS photocatalytic system. While, at pH 7, non-uniform shape of ZIS/CIS with rough surface formed. On the other hand, at pH 10.5 both smooth and rigid surface can be observed in ZIS/CIS photocatalytic system. Same observation can be seen also from TEM images (Fig. 3d–f). Even in ZIS/CIS-12.5 sample, the presence of CIS is distinguishable in the form of single dots on the ZIS surface (please refer to Fig. S2 for the SEM image of pristine ZIS) and around the ZIS particles (Fig. 3f). Additionally, layers in ZIS/CIS-7 (Fig. 3d) can be selected easily, while the layers in ZIS/CIS-12.5 were almost covered by CIS uniformly so that the layers were not noticeable easily.

Moreover, the obtained powder's optoelectronic characteristics also proved the differences between ZIS/CIS photocatalytic system. Fig. 4a shows, UV–vis absorption spectra of pristine ZIS and all other ZIS/CIS photocatalytic samples. As expected, all the ZIS/CIS samples showed red-shifted absorption edge as similar to the previous report on ZIS/CIS

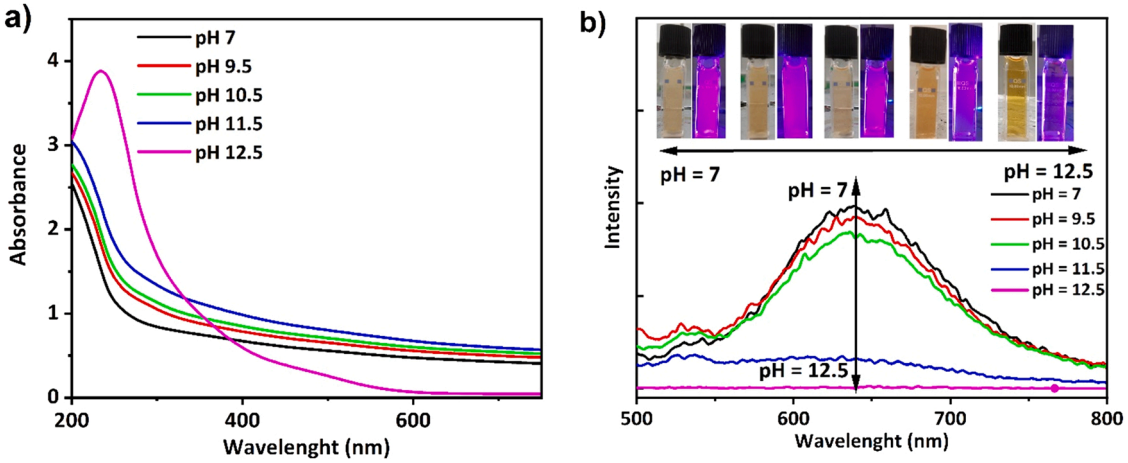

Fig. 1. a) UV–vis absorption spectrum of MUA capped CIS aggregates under different alkalinity levels (inset: The comparison of UV–vis absorption spectrum of MUA capped CIS and only MUA under pH = 7, 10.5 and 12.5. The dashed line represents UV–vis absorption spectrum of only MUA) and b) PL spectrum of CIS aggregates (λ excitation = 330 nm) at different alkalinity levels (inset: luminescence images of CIS aggregates under different alkalinity levels).

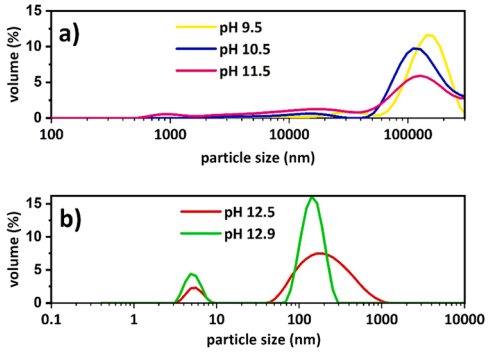

Fig. 2. CIS aggregates size distribution by DLS measurement under different alkaline levels a) pH 9.5–11.5 b) 12.5–12.9.

photocatalytic system [26]. However considerable red-shifting can be seen especially in ZIS/CIS-12.5 and ZIS/CIS-12.9 samples probably because of the uniform distribution of CIS on ZIS surface initiating the higher light harvesting due to the increase in surface-to-volume ratio. This is even observable from the significant color difference in obtained ZIS/CIS photocatalyst powder (Fig. S3). On the other hand, all samples' PL spectrum (Fig. 4b) have two characteristic peaks around 400–450 nm and 500–550 nm band which can be attributed to defects (sulfur and zinc vacancy) and band-to-band transition, respectively [43–45]. It is worth to mention that in all series of ZIS/CIS samples CIS decreased the electron-hole recombination efficiency in all ZIS/CIS samples as the lower PL intensity indicates lower recombination of photogenerated charge carriers [46].

Powder x-ray diffraction patterns (Fig. 5) for ZIS/CIS-7, ZIS/CIS-10.5, ZIS/CIS-12.5 and ZIS/CIS-12.9 shows the characteristic broad reflections were indexed by $ZnIn_2S_4$ that forms in a hexagonal crystal structure P63mc with reported lattice constants a = 3.871 Å and c = 26.121 Å. Expected positions for $ZnIn_2S_4$ phase are marked by the vertical bars. A XRD pattern for pristine $CuInS_2$ with tetragonal crystal structure in roquesite phase is presented in supplementary information (Fig. S4). The strongest broad reflections appear at 2Θ = 27.7, 46.3° and 19.9° and except the second one (2Θ = 46.3°) they overlap with the ZIS reflections and hence cannot be observed. The only impurity phase – In $(OH)_3$ marked by stars - appears for ZIS/CIS-12.9 sample.

In addition to this, more insight regarding samples' surface chemistry was also checked with FTIR (Fig. S5). All samples exhibited the same pattern. C-H strech vibration peaks located at 2844 and 2921 cm^{-1} indicates the alkyl chain orginated from the presence of CTAB molecule over ZIS/CIS and ZIS samples [47,48]. The peaks around 3415, 1620 and 1385 cm^{-1} corresponded to the hydroxyl and surface-absorbed water molecules, while the absorption peak related with the absorbed CO_2 molecules around 1100 cm^{-1} only can be seen in ZIS [49]. Interestingly In-S streching vibration orginated peak at around 640 cm^{-1} [49,50] can be seen all samples expect ZIS/CIS-7. This may be related with rough surface topology due to the overwhelmingly distributed CIS over ZIS surface as ZIS/CIS-10 and ZIS/CIS-12.5 with relatively more uniform CIS obtained that peak intensity is almost as high as in only ZIS especially in the case for ZIS/CIS-12.5.

PHE rates and the amount of hydrogen evolved from ZIS/CIS samples under visible light irradiation for 3 h in the presence of 0.35 M/0.25 M Na_2S/Na_2SO_3 as the sacrificial reagent can be seen in Fig. 6a and b, respectively. In Fig. 6a, black bars represent the PHE performances without in-situ Pt deposition, while red bars demonstrate with Pt. In case of the comparison of the samples' PHE rate without Pt, the highest rate was exhibited by ZIS/CIS-12.9 with 105.31 μmol g^{-1} h^{-1}. That result is reasonable as ZIS/CIS-12.9 was the only sample among all ZIS/CIS in which $In(OH)_3$ was formed during the preparation due to the high alkaline decoration medium (Fig. 5). Therefore, the presence of $In(OH)_3$ induced PHE performance of ZIS/CIS-12.9 remarkably as it has acted as a cocatalyst [11,51]. ZIS/CIS-7 and ZIS/CIS-9.5 showed very close PHE rate around 21.41 and 13.10 μmol g^{-1} h^{-1}, respectively. Around two folder PHE rate than ZIS/CIS-7 were achieved by ZIS/CIS-10.5 (55.65 μmol g^{-1} h^{-1}) and ZIS/CIS-11.5 (59.25 μmol g^{-1} h^{-1}). Interestingly, a notable decline was displayed in PHE rate from ZIS/CIS-12.5 (21.39 μmol g^{-1} h^{-1}). On the other hand, as the main scope of this study, the remarkable effect of the in-situ Pt deposition on PHE is readily observable in all ZIS/CIS/Pt samples. The lowest PHE rate was shown by ZIS/CIS-7/Pt (1180.46 μmol g^{-1} h^{-1}) and then ZIS/CIS-9.5/Pt (1300.46 μmol g^{-1} h^{-1}) whereas ZIS/CIS-10.5/Pt generated the highest amount of hydrogen with the rate of 1753.79 μmol g^{-1} h^{-1} which implies that the pH = 10.5 is the optimum pH level for the ZIS/CIS synthesis aqueous decoration medium that leading most efficient photocatalytic system for PHE. However, after reaching the optimum pH level for the decoration medium, PHE rate of the sample prepared in pH = 11.5 decreased to 1450.76 μmol g^{-1} h^{-1}. The significant rise can be seen from ZIS/CIS-12.5/Pt with the PHE rate of 1670.16 μmol g^{-1} h^{-1}. It seems that the optimum pH = 10.5 of the decoration of ZIS microspheres with CIS was the best for the hydrogen evolution from ZIS/CIS photocatalytic system in the presence of in-situ Pt deposition. Besides, the treatment of pristine ZIS or CIS sample in pH = 10.5 had no effect on PHE performance as almost the same amount of hydrogen was evolved from ZIS/Pt

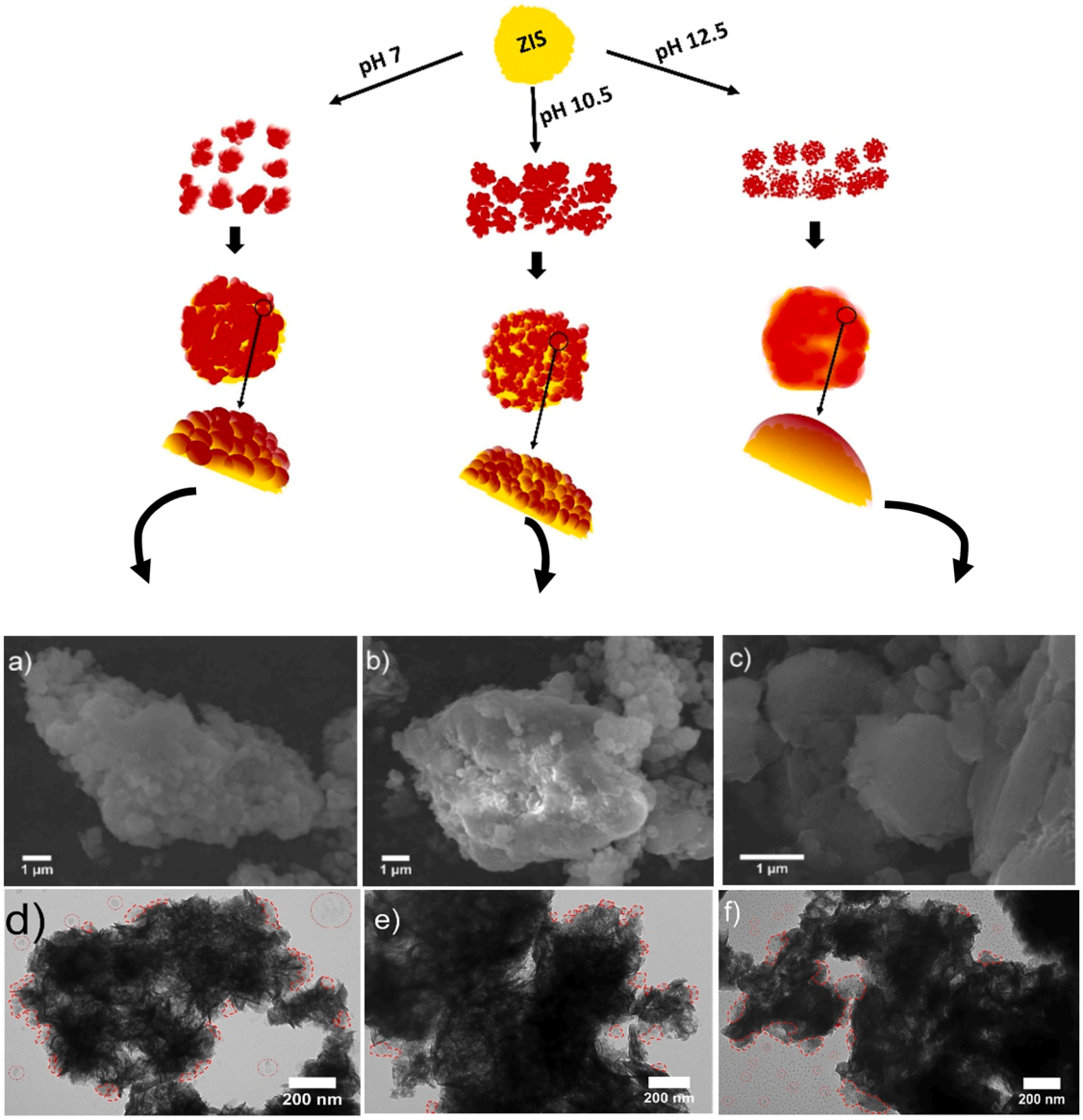

Fig. 3. Schematic description of controlled aggregation induced CIS (red spheres) decoration of ZIS microsphere (yellow sphere) based on SEM and TEM images of a, d) ZIS/CIS-7, b, e) ZIS/CIS-10.5 and c, f) ZIS/CIS-12.5. Red dashed circles in TEM images indicates CIS aggregates on and around the ZIS surface.

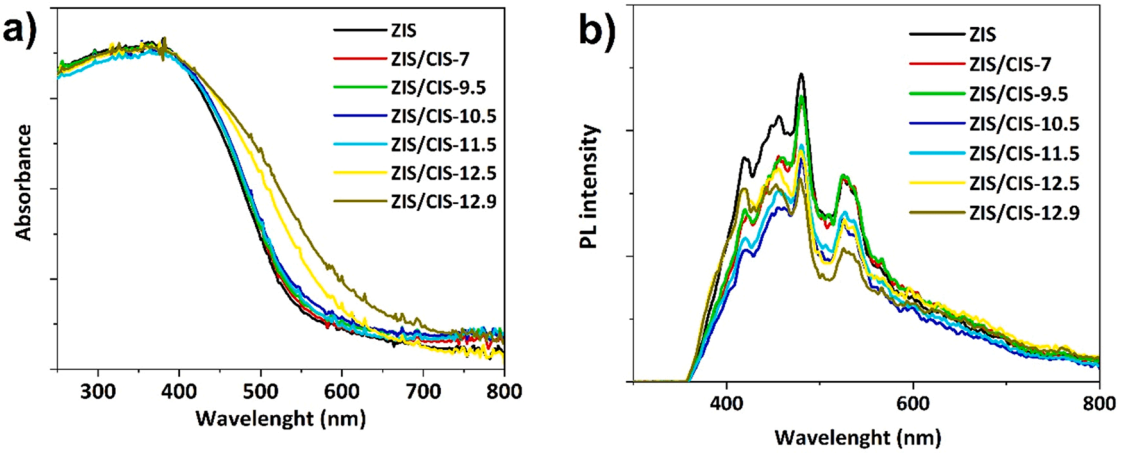

Fig. 4. a) UV–vis and b) PL spectrum of ZIS/CIS and pristine ZIS samples.

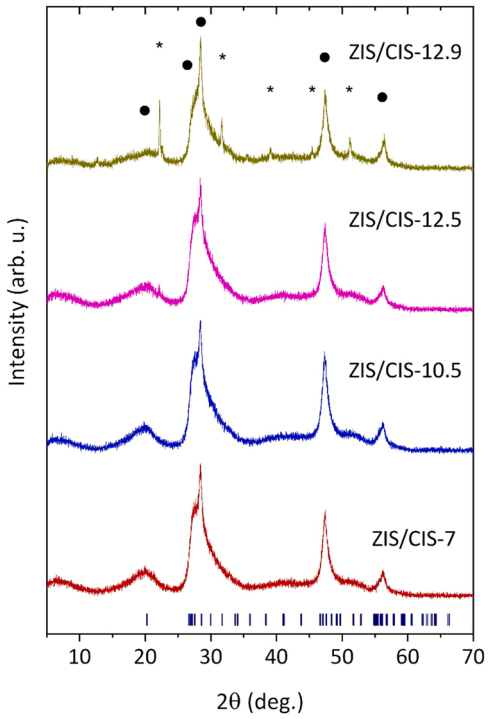

Fig. 5. XRD patterns of ZIS/CIS-7, 10.5, 12.5 and 12.9 samples. Dots and stars indicates the characteristic peaks in diffraction patterns originated from ZIS and In(OH)3, respectively.

with and without the treatment (Fig. S6). It is also worth to mention that ZIS/CIS-12.9/Pt exhibited PHE rate of 1512.58 μmol g^{-1} h^{-1} but the competition between the electron transfer from ZIS/CIS to two cocatalyst Pt species and $In(OH)_3$ could inhibit the performance of ZIS/CIS-12.9/Pt in comparison to ZIS/CIS-12.5/Pt [52]. Fig. 6c. shows the recycling performance experiments of three selected samples: ZIS/CIS-7/Pt, ZIS/CIS-10.5/Pt and ZIS/CIS-12.5/Pt (The reason of that selection will be discussed further). The samples were not stable after 3 cycles as a drop about 60 % in PHE for ZIS/CIS-10.5/Pt and ZIS/CIS-12.5/Pt was observed while around 30 % for ZIS/CIS-7. Particularly, around 50 % rapid decline was observed from ZIS/CIS-10.5/Pt at the end of 2nd cycle. Higher stability in ZIS/CIS-7/Pt comparing to ZIS/CIS-10.5/Pt might be attributed to the relatively larger CIS aggregates in ZIS/CIS-7 which are somehow lesser prone to photocorrosion in ZIS/CIS photocatalytic system. On the other hand, the core-shell like structure in ZIS/CIS-12.5 exhibited higher photostability than that of ZIS/CIS-10.5 which indicates the stronger interaction between ZIS and CIS in ZIS/CIS-12.5 can be more beneficial for the stability of ZIS/CIS photocatalytic system. Lastly, additional second PHE tests were carried out over those selected samples (Fig. S7) to affirm the above-mentioned PHE results. Very close PHE evolution performance was proven from ZIS/CIS-10.5/Pt and ZIS/CIS-12.5/Pt whereas ZIS/CIS-7/Pt exhibited lowest performance among the selected samples.

To acquire more insight to reveal the reason behind PHE activity, the three key samples ZIS/CIS-7, 10.5 and 12.5 was highlighted. This is because of the above-mentioned characteristic of CIS under different decoration medium resulting in different aggregation properties of CIS. The decoration under pH = 7 and 10.5 led to CIS aggregates with aggregation induced emission property and CIS under pH = 12.5 was relatively more uniformly dispersed with quenched emission while keeping the polydispersity. To further verify photocatalytic reducing power ability of selected ZIS/CIS samples, photocatalytic methyl viologen (MV^{2+}) reduction to radical ($MV^{+\bullet}$) was carried out (Fig. 7) to investigate the difference in reducing power ability (E ($MV^{2+}/MV^{+\bullet}$) = −0.44 V vs. NHE, pH 7) [53,54]. After 9 min the irradiation under λ = 420 nm, a change in color from yellow to dark blue as an indication of $MV^{+\bullet}$ generation [55–57] was observed from all samples proving that all samples' photogenerated electrons are sufficient for MV^{+2} reduction [58]. Moreover, UV–vis absorption spectra of all samples displayed a characteristic peak at 605 nm corresponding to $MV^{+\bullet}$ [59]. The highest radical generation was observed from ZIS/CIS-10.5 that similar result as in PHE activity. However, ZIS/CIS-7 produced higher $MV^{+\bullet}$ than that of ZIS/CIS-12.5 that is incompatible with the trend as in PHE result. This could be related with the adsorption of MV^{2+} which is more favorable on S-terminated surfaces with electron rich sulfur ions due to the positively charged nitrogens on MV^{2+} with poor electron [60]. Consequently, the uniform coating like coupling of MUA capped CIS over ZIS surface in ZIS/CIS-12.5 could block sulfur rich S-terminated surface in ZIS microspheres resulting in the poorest adsorption of MV^{2+} in comparison with ZIS/CIS-7 and ZIS/CIS-10.5. Therefore, it would be sensible to make comparison between only ZIS/CIS-7 and ZIS/CIS-10.5 in which ZIS/CIS-10.5 has higher reducing power ability than that of ZIS/CIS-7.

Optimization of the amount of Pt over photocatalytic systems is required to achieve the highest PHE rate [61,62]. However, the type of Pt species formed during in-situ deposition are very crucial as well as the amount and the formation of the Pt species [63]. Besides, the content of Pt species in ZIS/CIS can give an insight about PHE performances of selected samples. To confirm this supposition, firstly the percentage of weight loading of Pt in collected three selected samples after PHE tests were confirmed by ICP-OES technique (Table 1). Then the XPS technique was used to analyze the chemical composition of the selected samples (Table 1 and Table S1).

Indeed, the recorded Pt 4 f and O 1 s HR spectra confirm the presence of Pt-$(OH)_x$, Pt-Ox and Pt-Sx species [26,64] over ZIS/CIS-7/Pt,

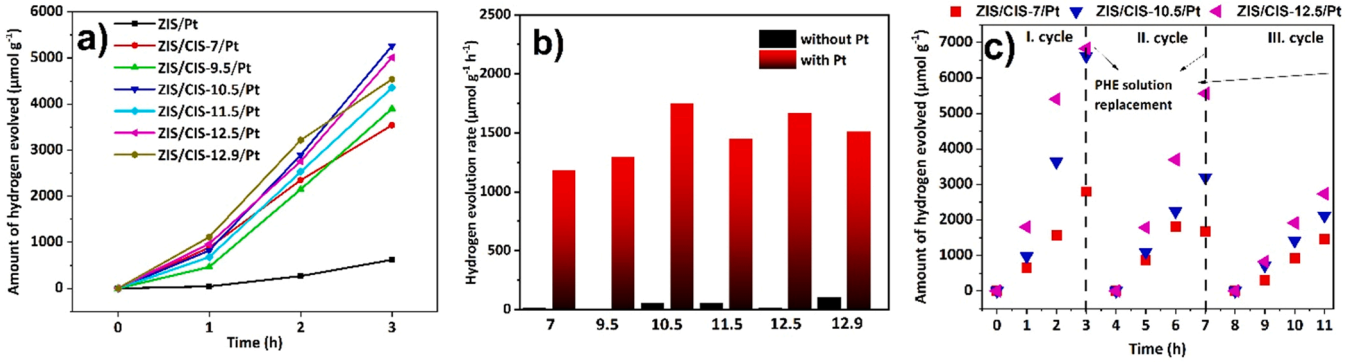

Fig. 6. a) Amount of evolved hydrogen with Pt deposition and b) hydrogen evolution rate by ZIS and ZIS/CIS samples with and without in-situ Pt deposition (7, 9.5, 10.5, 11.5, 12.5 and 12.9 represent ZIS/CIS-7, ZIS/CIS-9.5, ZIS/CIS-10.5, ZIS/CIS-11.5, ZIS/CIS-12.5 and ZIS/CIS-12.9, respectively) c) Recycling performance of three selected samples ZIS/CIS-7, ZIS/CIS-10.5 and ZIS/CIS-12.5.

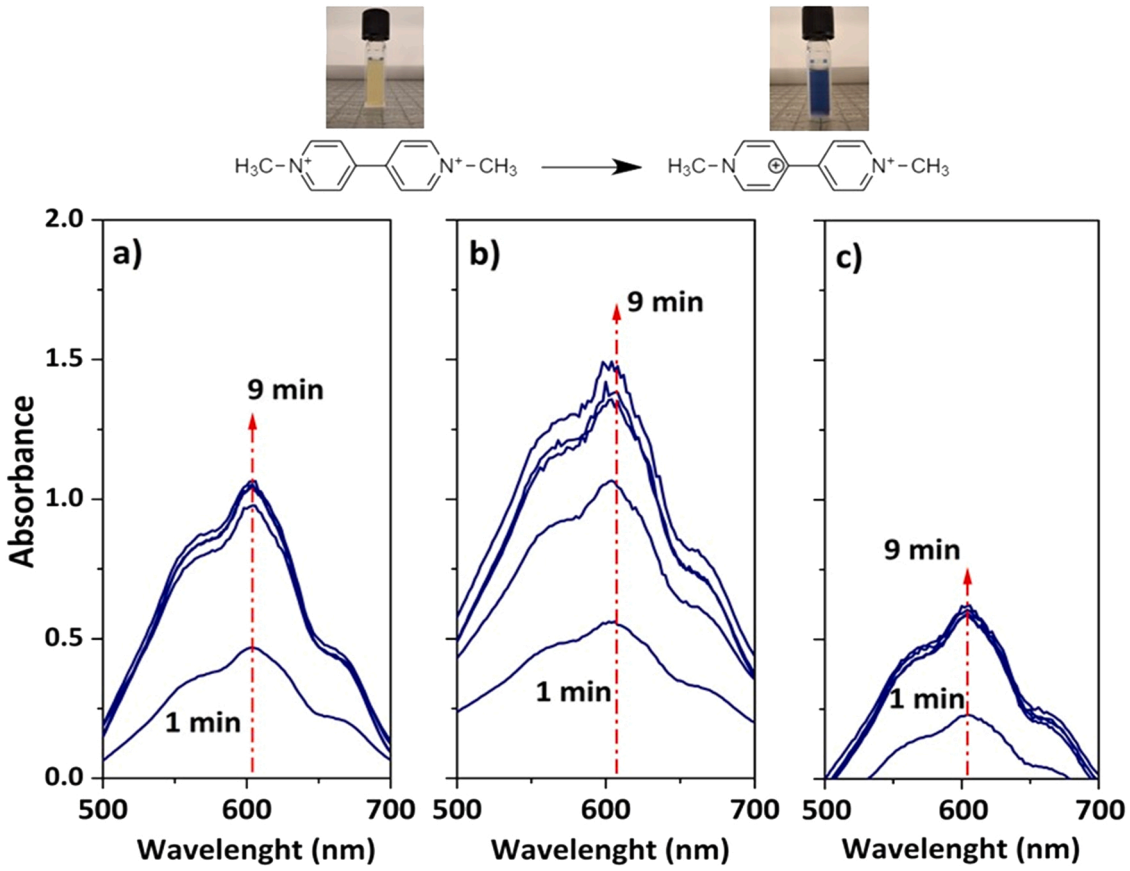

Fig. 7. Normalized UV–vis spectra originated from photoreduction of methyl viologen (MV2 +) over a 3 ml mixture composed of a) ZIS/CIS- 7, b) ZIS/CIS-10.5 and c) ZIS/CIS-12.5 samples (0.5 mg/ml), methyl viologen dichloride, [MV2+] = 1.8 mM and sacrifacial reagent Na2S/Na2SO3 (0.35 M/0.25 M). Prior to the monochromatic light irradiation λ = 420 nm, the mixture was purged with N2 gas with 4 dm3/h flow rate for 4 min to remove the O2 from the system to prevent the reoxidation of MV+•. Inset image shows the color change of mixture from yellow to dark blue as an indication of MV+•.

Table 1
ICP-OES, XPS analysis of ZIS/CIS-7/Pt, 10.5/Pt and 12.5/Pt samples and their PHE rate.

Sample	ICP-OES		XPS			PHE rate (μmol g^{-1} h^{-1})
	Cu (wt%)	Pt (wt %)	Pt-CO,Pt-CxHy (%)	Pt-OH, Pt-Ox, Pt-Sx (%)	Pt content (at %)	
ZIS/CIS-7/Pt	0.36	0.36	30.40	69.60	0.21	1180.46
ZIS/CIS-10.5/Pt	0.39	0.20	27.14	72.86	0.26	1753.79
ZIS/CIS-12.5/Pt	0.39	0.25	30.72	69.28	0.18	1670.16

ZIS/CIS-10.5/Pt and ZIS/CIS-12.5/Pt samples (Fig. 8) and highly likely originated from $Pt(OH)_2$ that will be explained later. Moreover, the highest content of those Pt species was identified for the ZIS/CIS-10.5/Pt sample (Table 1) that is around more than 3 % higher than that of ZIS/CIS-7/Pt and ZIS/CIS-12.5/Pt samples. Similar minor difference in oxidative species was also reported elsewhere where 2 % higher oxidative species resulted in significantly higher electrocatalytic hydrogen evolution performance in alkaline media [65].

It is known that, highly alkaline aqueous solution in PHE solution can be formed (pH = 13) because of the formation of bisulfide ion HS^- and HSO_3^- from Na_2S/Na_2SO_3 through the hydrolysis [66] (Eqs. (1) and (2)):

$$S^{2-} + H_2O \rightarrow HS^- + OH^- \quad (1)$$

$$SO_3^{2-} + H_2O \rightarrow HSO_3^- + OH^- \quad (2)$$

Therefore, displacement of Cl^- from $PtCl_4^{2-}$ by OH^- takes place resulted in $Pt(OH)_2$ by the adsorption of $PtCl_4^{2-}$ on OH^- on ZIS/CIS surface leading the formation of $Pt(OH)_2$ taking place before the light irradiation during the nitrogen purging (Eq. (3)):

$$PtCl_4^{2-} + 2OH^- \rightarrow Pt(OH)_2 + 4Cl^- \quad (3)$$

As acidic conditions are suitable for the formation of Pt-Sx, the formation of Pt-Sx species are unlikely under high pH of PHE solution (pH = 13) [67]. On the other hand, Pt-C_xH_x and Pt-CO species might reveal the simultaneous formation of metallic Pt^0 on ZIS/CIS surface during the visible light irradiation induced PHE [68] (Eqs. (4) and (5)).

$$ZIS/CIS + h\nu \rightarrow e^-_{CB} + h^+_{VB} \quad (4)$$

$$Pt^{2+} + 2e^- \rightarrow Pt^0 \quad (5)$$

However, it is worth to note that the proximity in binding energies (BE) of Pt^0 and Pt with the Cu, CO and CxHx chemical environment make difficult to predict the exact oxidation state whether is zero or close the zero.

Supposedly, PHE evolution over ZIS/CIS sample were initiated by $Pt(OH)_2$ species, and taking into consideration that the formation of $Pt(OH)_2$ occurs before the light irradiation as above-mentioned, $PtCl_4^{2-}$ complex ion interaction with ZIS/CIS surface before the light irradiation should be pointed out. For that purpose, ζ-potentials of the selected samples was investigated in the PHE solution. Expectedly, the surfaces of

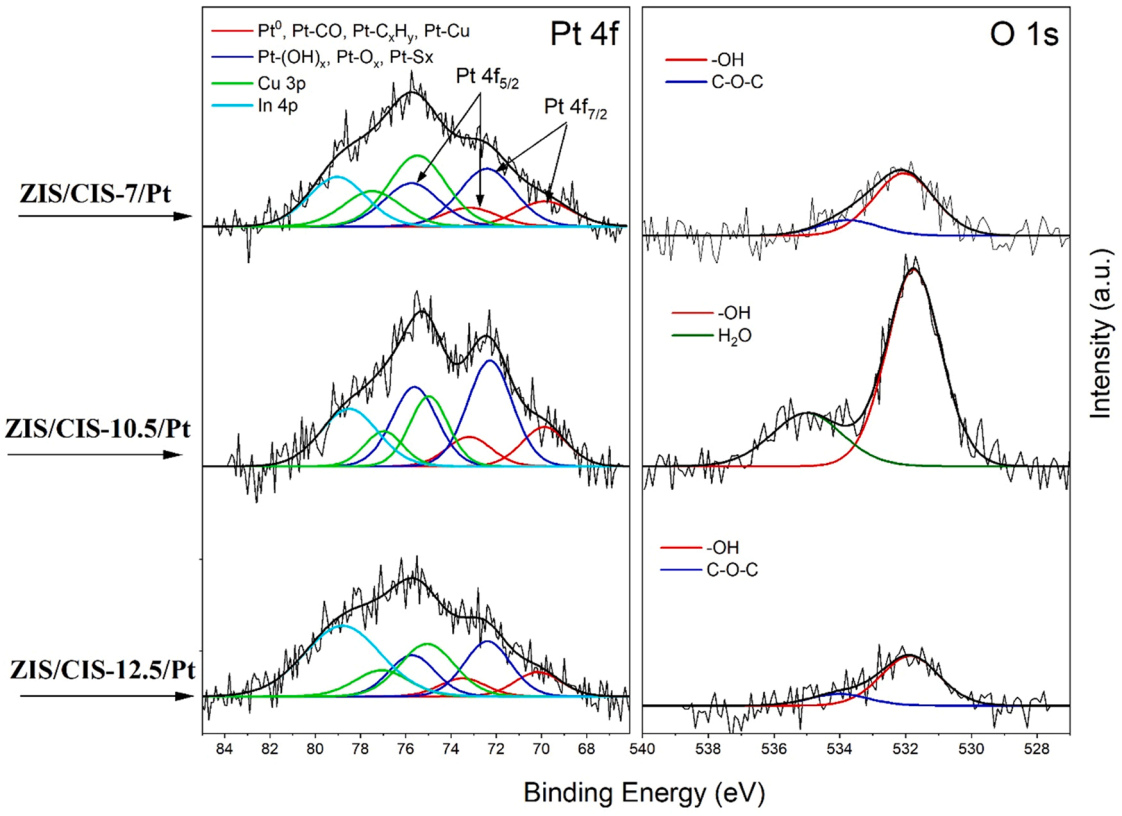

Fig. 8. XPS High resolution Pt 4f and O 1s XPS spectra recorded on ZIS/CIS-7/Pt, ZIS/CIS-10.5/Pt and ZIS/CIS-12.5/Pt photocatalytic systems after PHE tests. Deconvoluted peaks of Pt species are overlapped by Cu 3p and In 4p signals.

ZIS/CIS-7, 10.5 and 12.5 were negatively charged with a ζ-potential of -18.3 ± 0.60, 15.56 ± 0.58 and -14.46 ± 0.43 mV, respectively (Fig. S8). ζ-potential of the samples decreases as their decoration medium pH increase. Comparing with ZIS/CIS-7, Pt^{2+} cations from $PtCl_4^{2-}$ complex ion can be adsorbed relatively harder over ZIS/CIS-10.5 surface than that of ZIS/CIS-7 by electrostatic interactions. Yet, the difference in ζ-potential is little, thereby it might have no decisive role in the difference between PHE performances.

Consequently, the overall mechanism from before light irradiation to PHE process can be proposed as follows (Fig. 9); (1) hydrolysis of Na_2S/Na_2SO_3 sacrifacial reagent results in formation of OH^- (2) which is adsorbed by the ZIS/CIS surface and displace the chloride ligands in $PtCl_4^{2-}$ complex ion. Upon the visible light irradiation, (3) photogenerated electrons and holes over ZIS/CIS transferring across p-n junction mechanism similar to the reports elsewhere [23,26] in accordance to the conduction (CB) and valance band (VB) alignment in ZIS ($CB_{ZIS} = -0.99$ eV, $VB_{ZIS} = 1.5$ eV) and CIS ($CB_{CIS} = -1.27$ eV, $VB_{CIS} = 0.6$ eV) [26] leading to (4) three different simultaneous reaction including reduction of Pt(II) to Pt(0), PHE hydrogen evolution over Pt $(OH)_2$ and simultaneously formed metallic Pt, and oxidation of sacrifacial reagent by photogenerated holes. In addition, it is worth clarifying the effect of the morphology of CIS in ZIS/CIS photocatalytic systems on

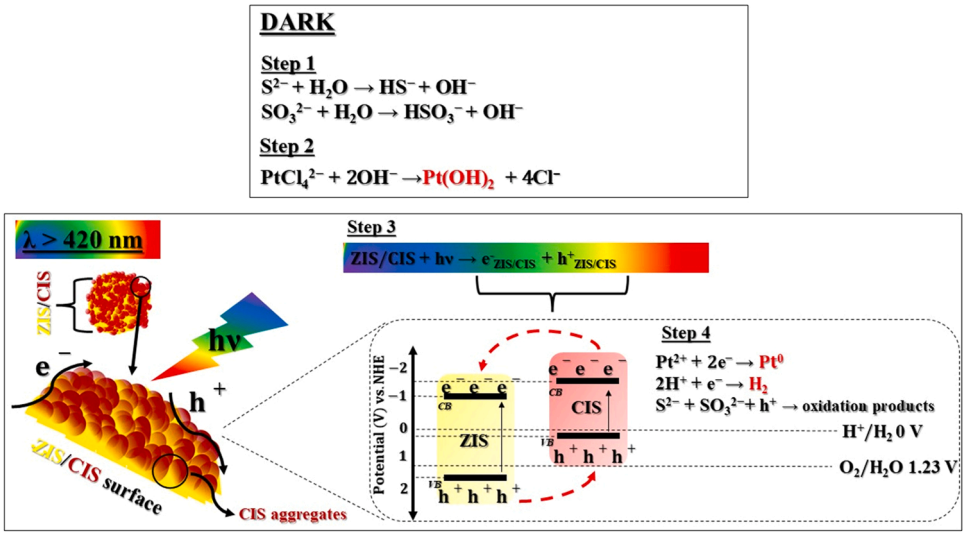

Fig. 9. Overall PHE mechanism before and after the light irradiation illustrated step-by-step.

PHE performance. Based on UV–vis spectra (Fig. 4), the significantly improved light harvesting property in ZIS/CIS-12.5 might be responsible for the sudden increased trend in PHE performance in ZIS/CIS-12.5/Pt (Fig. 6b). However, as PL spectra is a useful tool to explore the charge separation of the photogenerated electron-hole carriers [69–71], the lower recombination was observed in ZIS/CIS-10.5 compared to ZIS/CIS-12.5 (Fig. 4). That can be interpreted in terms of the presence of CIS in a form of single quantum size in core-shell like ZIS/CIS-12.5 photocatalytic system [72]. At this amount (5 wt%) of CIS in this photocatalytic system might act as a recombination center that inhibits the electron transfer reducing the PHE performance. On the other hand, it was not the case for ZIS/CIS-10.5 in which core-shell structure was not obtained and the contact between ZIS and CIS was poorer. Thus, lower recombination of charge carriers was observed in ZIS/CIS-10.5 Therefore, although the light harvesting property is lower in ZIS/CIS-10.5 than that of ZIS/CIS-12.5, the recombination is higher in ZIS/CIS-12.5. As a result, taken together with the Pt species factor and the optimum balance between light harvesting and charge recombination property, the most suitable condition for PHE was achieved in ZIS/CIS-10.5/Pt among other prepared ZIS/CIS photocatalytic systems.

4. Conclusion

The controlled aggregation of the photoluminescent CIS QDs over hydrothermally obtained ZIS surface in aqueous media was initiated by the mercaptocarboxylic acid capping ligand by adjusting the alkalinity level of aqueous decoration medium. Despite the same amount of CIS decoration (5 wt%) and in-situ Pt deposition (0.5 wt%) in prepared ZIS/CIS photocatalytic samples, their photocatalytic hydrogen evolution performances after 3 h of visible light irradiation ($\lambda > 420$ nm) differed significantly. Optimum aggregation control for the highest amount of hydrogen evolution rate from ZIS/CIS-10.5/Pt was higher than that of ZIS/CIS-7/Pt and ZIS/CIS-12.5/Pt where CIS formed uniform surface topology over ZIS surface. Those results remark the importance of the surface chemical states of most popular cocatalyst Pt noble metal which was supported by the XPS analysis revealing that ZIS/CIS-10.5 exhibited the highest content of Pt-Ox and Pt-$(OH)_x$ species in comparison with ZIS/CIS-7 and ZIS/CIS-12.5. Moreover, a similar trend was also confirmed by the monochromatic light irradiation ($\lambda = 420$ nm) induced methyl viologen (MV^{2+}) photoreduction to radical ($MV^{+\bullet}$) over samples in Na_2S/Na_2SO_3 (0.35 M/0.25 M) aqueous solution confirming that ZIS/CIS-10.5 reduced highest amount of MV^{2+} to $MV^{+\bullet}$ implying the reducing power is the highest in ZIS/CIS-10.5.

This work indicates the importance of the surface chemistry and the topology in photocatalytic system's hydrogen evolution performances that requires Pt cocatalyst that is essential for the sustainable hydrogen economy.

CRediT authorship contribution statement

Onur Cavdar: Conceptualization, Methodology, Investigation, Validation, Visualization, Writing – original draft. **Anna Malankowska:** Funding acquisition, Supervision, Conceptualization, Resources, Writing – review & editing. **Justyna Łuczak:** Methodology. **Andrzej Żak:** Investigation. **Wojciech Lisowski:** Investigation, Writing – original draft. **Tomasz Klimczuk**: Investigation, Writing – original draft. **Adriana Zaleska-Medynska:** Resources, Writing – review & editing.

Declaration of Competing Interest

The authors declare that they have no known competing financial interests or personal relationships that could have appeared to influence the work reported in this paper.

Data Availability

Data will be made available on request.

Acknowledgements

This research was financially supported by National Science Centre, Poland (Grant No. 2016/23/D/ST8/02682).

Appendix A. Supporting information

Supplementary data associated with this article can be found in the online version at doi:10.1016/j.colsurfa.2022.129760.

References

[1] J.O. Abe, A.P.I. Popoola, E. Ajenifuja, O.M. Popoola, Hydrogen energy, economy and storage: review and recommendation, Int. J. Hydrogen Energy 44 (2019) 15072–15086, https://doi.org/10.1016/j.ijhydene.2019.04.068.
[2] J. Qi, W. Zhang, R. Cao, Solar-to-hydrogen energy conversion based on water splitting, Adv. Energy Mater. 8 (2018) 1–16, https://doi.org/10.1002/aenm.201701620.
[3] K. Zhang, L. Guo, Metal sulphide semiconductors for photocatalytic hydrogen production, Catal. Sci. Technol. 3 (2013) 1672–1690, https://doi.org/10.1039/c3cy00018d.
[4] A. Amedeo, N. Yifat, A. Lilac, B. Giacomo, Photosynthetic H_2 generation and organic transformations with CdSe@CdS-Pt nanorods for highly efficient solar-to-chemical energy conversion, Nano Energy 70 (2020), 104510, https://doi.org/10.1016/j.nanoen.2020.104510.
[5] S. Bojja, U. Pal, T.P. Yendrapati, J. Soumya, Robust Co_9S_8@$CdIn_2S_4$ cage for efficient photocatalytic H_2 evolution, J. Phys. Chem. C 125 (2021) 5099–5109, https://doi.org/10.1021/acs.jpcc.0c11554.
[6] R. Bariki, D. Majhi, K. Das, A. Behera, B.G. Mishra, Facile synthesis and photocatalytic efficacy of UiO-66/$CdIn_2S_4$ nanocomposites with flowerlike 3D-microspheres towards aqueous phase decontamination of triclosan and H_2 evolution, Appl. Catal. B Environ. 270 (2020), 118882, https://doi.org/10.1016/j.apcatb.2020.118882.
[7] Y. Li, J. Wang, S. Peng, G. Lu, S. Li, Photocatalytic hydrogen generation in the presence of glucose over ZnS-coated $ZnIn_2S_4$ under visible light irradiation, Int. J. Hydrogen Energy 35 (2010) 7116–7126, https://doi.org/10.1016/j.ijhydene.2010.02.017.
[8] M. Tabata, K. Maeda, T. Ishihara, T. Minegishi, T. Takata, K. Domen, Photocatalytic hydrogen evolution from water using copper gallium sulfide under visible-light irradiation, J. Phys. Chem. C 114 (2010) 11215–11220, https://doi.org/10.1021/jp103158f.
[9] J. Wang, S. Sun, R. Zhou, Y. Li, Z. He, H. Ding, et al., A review: synthesis, modification and photocatalytic applications of $ZnIn_2S_4$, J. Mater. Sci. Technol. 78 (2021) 1–19, https://doi.org/10.1016/j.jmst.2020.09.045.
[10] H. Liu, J. Zhang, D. Ao, Construction of heterostructured $ZnIn_2S_4$@NH_2-MIL-125 (Ti) nanocomposites for visible-light-driven H_2 production, Appl. Catal. B Environ. 221 (2018) 433–442, https://doi.org/10.1016/j.apcatb.2017.09.043.
[11] M. Geng, Y. Peng, Y. Zhang, X. Guo, F. Yu, X. Yang, et al., Hierarchical $ZnIn_2S_4$: a promising cocatalyst to boost visible-light-driven photocatalytic hydrogen evolution of $In(OH)_3$, Int. J. Hydrogen Energy 44 (2019) 5787–5798, https://doi.org/10.1016/j.ijhydene.2019.01.094.
[12] C. Zhao, Y. Zhang, H. Jiang, J. Chen, Y. Liu, Q. Liang, et al., Combined effects of octahedron NH_2-UiO-66 and Flowerlike $ZnIn_2S_4$ microspheres for photocatalytic dye degradation and hydrogen evolution under visible light, J. Phys. Chem. C 123 (2019) 18037–18049, https://doi.org/10.1021/acs.jpcc.9b03807.
[13] D. Kong, H. Fan, D. Yin, D. Zhang, X. Pu, S. Yao, et al., $AgFeO_2$ nanoparticle/$ZnIn_2S_4$ microsphere p-n heterojunctions with hierarchical nanostructures for efficient visible-light-driven H2Evolution, ACS Sustain. Chem. Eng. 9 (2021) 2673–2683, https://doi.org/10.1021/acssuschemeng.0c07638.
[14] G. Zuo, Y. Wang, W.L. Teo, A. Xie, Y. Guo, Y. Dai, et al., Ultrathin $ZnIn_2S_4$ nanosheets anchored on Ti_3C_2TX MXene for photocatalytic H 2 evolution, Angew. Chem. 132 (2020) 11383–11388, https://doi.org/10.1002/ange.202002136.
[15] Z. Li, X. Wang, W. Tian, A. Meng, L. Yang, CoNi bimetal cocatalyst modifying a hierarchical $ZnIn_2S_4$ nanosheet-based microsphere noble-metal-free photocatalyst for efficient visible-light-driven photocatalytic hydrogen production, ACS Sustain Chem. Eng. 7 (2019), https://doi.org/10.1021/acssuschemeng.9b06430, 20190–201.
[16] Z. Gao, K. Chen, L. Wang, B. Bai, H. Liu, Q. Wang, Aminated flower-like $ZnIn_2S_4$ coupled with benzoic acid modified g-C_3N_4 nanosheets via covalent bonds for ameliorated photocatalytic hydrogen generation, Appl. Catal. B Environ. 268 (2020), 118462, https://doi.org/10.1016/j.apcatb.2019.118462.
[17] J. Liu, G. Chen, J. Sun, Ag_2S-modified $ZnIn_2S_4$ nanosheets for photocatalytic H_2 generation, ACS Appl. Nano Mater. 3 (2020) 11017–11024, https://doi.org/10.1021/acsanm.0c02240.
[18] Y. Chen, Z. Qin, X. Wang, X. Guo, L. Guo, Noble-metal-free Cu2S-modified photocatalysts for enhanced photocatalytic hydrogen production by forming

nanoscale p-n junction structure, RSC Adv. 5 (2015) 18159–18166, https://doi.org/10.1039/c5ra00091b.
[19] E. Zhang, Q. Zhu, J. Huang, J. Liu, G. Tan, C. Sun, et al., Visually resolving the direct Z-scheme heterojunction in CdS@ ZnIn2S4 hollow cubes for photocatalytic evolution of H2 and H2O2 from pure water, Appl. Catal. B Environ. 293 (2021), 120213, https://doi.org/10.1016/j.apcatb.2021.120213.
[20] W. Li, Z. Lin, G. Yang, A 2D self-assembled $MoS_2/ZnIn_2S_4$ heterostructure for efficient photocatalytic hydrogen evolution, Nanoscale 9 (2017) 18290–18298, https://doi.org/10.1039/c7nr06755k.
[21] W. Pudkon, S. Kaowphong, S. Pattisson, P.J. Miedziak, H. Bahruji, T.E. Davies, et al., Microwave synthesis of $ZnIn_2S_4/WS_2$ composites for photocatalytic hydrogen production and hexavalent chromium reduction, Catal. Sci. Technol. 9 (2019) 5698–5711, https://doi.org/10.1039/c9cy01553a.
[22] X. Guo, Y. Peng, G. Liu, G. Xie, Y. Guo, Y. Zhang, et al., An efficient $ZnIn_2S_4$@ $CuInS_2$ core–shell p–n heterojunction to boost visible-light photocatalytic hydrogen evolution, J. Phys. Chem. C 124 (2020) 5934–5943, https://doi.org/10.1021/acs.jpcc.9b11623.
[23] Z. Guan, J. Pan, Q. Li, G. Li, J. Yang, Boosting visible-light photocatalytic hydrogen evolution with an efficient $CuInS_2/ZnIn_2S_4$ 2D/2D heterojunction, ACS Sustain. Chem. Eng. 7 (2019) 7736–7742, https://doi.org/10.1021/acssuschemeng.8b06587.
[24] A. Raja, N. Son, M. Swaminathan, M. Kang, Facile synthesis of sphere-like structured $ZnIn_2S_4$-rGO-$CuInS_2$ ternary heterojunction catalyst for efficient visible-active photocatalytic hydrogen evolution, J. Colloid Interface Sci. 602 (2021) 669–679, https://doi.org/10.1016/j.jcis.2021.06.034.
[25] Z. Long, W. Zhang, J. Tian, G. Chen, Y. Liu, R. Liu, Recent research on the luminous mechanism, synthetic strategies, and applications of $CuInS_2$ quantum dots, Inorg. Chem. Front. 8 (2021) 880–897, https://doi.org/10.1039/D0QI01228A.
[26] O. Cavdar, A. Malankowska, D. Amgar, P. Mazierski, J. Łuczak, W. Lisowski, et al., Remarkable visible-light induced hydrogen generation with $ZnIn_2S_4$ microspheres/ $CuInS_2$ quantum dots photocatalytic system, Int. J. Hydrogen Energy 46 (2020) 486–498, https://doi.org/10.1016/j.ijhydene.2020.09.212.
[27] M. Mou, Y. Wu, Q. Niu, Y. Wang, Z. Yan, S. Liao, Aggregation-induced emission properties of hydrothermally synthesized Cu-In-S quantum dots, Chem. Commun. 53 (2017) 3357–3360, https://doi.org/10.1039/c7cc00170c.
[28] Y. Zhang, L. Mi, P.N. Wang, J. Ma, J.Y. Chen, pH-dependent aggregation and photoluminescence behavior of thiol-capped CdTe quantum dots in aqueous solutions, J. Lumin 128 (2008) 1948–1951, https://doi.org/10.1016/j.jlumin.2008.06.004.
[29] V. Swayambunathan, D. Hayes, K.H. Schmidt, Y.X. Liao, D. Meisel, Thiol surface complexation on growing CdS clusters, J. Am. Chem. Soc. 112 (1990) 3831–3837, https://doi.org/10.1021/ja00166a017.
[30] S. Xu, C. Wang, H. Zhang, Z. Wang, B. Yang, Y. Cui, PH-sensitive photoluminescence for aqueous thiol-capped CdTe nanocrystals, Nanotechnology (2011) 22, https://doi.org/10.1088/0957-4484/22/31/315703.
[31] S. Yu, Z.J. Li, X.B. Fan, J.X. Li, F. Zhan, X.B. Li, et al., Vectorial electron transfer for improved hydrogen evolution by mercaptopropionic-acid-regulated CdSe quantum-dots-TiO_2-$Ni(OH)_2$ assembly, ChemSusChem 8 (2015) 642–649, https://doi.org/10.1002/cssc.201402885.
[32] C.M. Chang, K.L. Orchard, B.C.M. Martindale, E. Reisner, Ligand removal from CdS quantum dots for enhanced photocatalytic H_2 generation in pH neutral water, J. Mater. Chem. A 4 (2016) 2856–2862, https://doi.org/10.1039/c5ta04136h.
[33] Y. Park, W. Kim, D. Monllor-Satoca, T. Tachikawa, T. Majima, W. Choi, Role of interparticle charge transfers in agglomerated photocatalyst nanoparticles: demonstration in aqueous suspension of dye-sensitized TiO_2, J. Phys. Chem. Lett. 4 (2013) 189–194, https://doi.org/10.1021/jz301881d.
[34] Y.J. Gao, Y. Yang, X.B. Li, H.L. Wu, S.L. Meng, Y. Wang, et al., Self-assembled inorganic clusters of semiconducting quantum dots for effective solar hydrogen evolution, Chem. Commun. 54 (2018) 4858–4861, https://doi.org/10.1039/c8cc02091d.
[35] K. Sawaguchi-Sato, A. Kobayashi, M. Yoshida, M. Kato, Aggregation-enhanced photocatalytic H_2 evolution activity of photosensitizing cadmium selenide quantum dots and platinum colloidal catalysts, J. Photochem. Photobiol. A Chem. 335 (2017) 182–189, https://doi.org/10.1016/j.jphotochem.2016.11.028.
[36] M.C. Nevárez Martínez, O. Cavdar, Haliński ŁP, M. Miodyńska, P. Parnicka, B. Bajorowicz, et al., Hydrogen detection during photocatalytic water splitting: a tutorial, Int. J. Hydrogen Energy (2022), https://doi.org/10.1016/j.ijhydene.2022.03.050.
[37] Y. Liang, J.E. Thorne, B.A. Parkinson, Controlling the electronic coupling between CdSe quantum dots and thiol capping ligands via pH and ligand selection, Langmuir 28 (2012) 11072–11077, https://doi.org/10.1021/la301237p.
[38] J. Moon, K. Choi, B. Kim, K. Yoon, T. Seong, K. Woo, Aggregation-free process for functional CdSe/CdS core/shell quantum dots, J. Phys. Chem. C (2009) 7114–7119.
[39] W. Jiang, S. Mardyani, H. Fischer, W.C.W. Chan, Design and characterization of lysine cross-linked mercapto-acid biocompatible quantum dots, Chem. Mater. 18 (2006) 872–878, https://doi.org/10.1021/cm051393.
[40] H.T. Uyeda, I.L. Medintz, J.K. Jaiswal, S.M. Simon, H. Mattoussi, Synthesis of compact multidentate ligands to prepare stable hydrophilic quantum dot fluorophores, J. Am. Chem. Soc. 127 (2005) 3870–3878, https://doi.org/10.1021/ja044031w.
[41] T. Laaksonen, P. Ahonen, C. Johans, K. Kontturi, Stability and electrostatics of mercaptoundecanoic acid-capped gold nanoparticles with varying counterion size, ChemPhysChem 7 (2006) 2143–2149, https://doi.org/10.1002/cphc.200600307.
[42] C. Wei, X. Wei, Z. Hu, D. Yang, S. Mei, G. Zhang, et al., A fluorescent probe for Cd^{2+} detection based on the aggregation-induced emission enhancement of aqueous Zn-Ag-In-S quantum dots, Anal. Methods 11 (2019) 2559–2564, https://doi.org/10.1039/c9ay00716d.
[43] S. Shen, P. Guo, L. Zhao, Y. Du, L. Guo, Insights into photoluminescence property and photocatalytic activity of cubic and rhombohedral $ZnIn_2S_4$, J. Solid State Chem. 184 (2011) 2250–2256, https://doi.org/10.1016/j.jssc.2011.06.033.
[44] J. Ding, C. Zheng, L. Wang, C. Lu, B. Zhang, Y. Chen, et al., Viologen-inspired functional materials: Synthetic strategies and applications, J. Mater. Chem. A 7 (2019) 23337–23360, https://doi.org/10.1039/c9ta01724k.
[45] S. Shen, L. Zhao, X. Guan, L. Guo, Improving visible-light photocatalytic activity for hydrogen evolution over $ZnIn_2S_4$: a case study of alkaline-earth metal doping, J. Phys. Chem. Solids 73 (2012) 79–83, https://doi.org/10.1016/j.jpcs.2011.09.027.
[46] C. Liu, Y. Zhang, J. Wu, H. Dai, C. Ma, Q. Zhang, et al., Ag-Pd alloy decorated $ZnIn_2S_4$ microspheres with optimal Schottky barrier height for boosting visible-light-driven hydrogen evolution, J. Mater. Sci. Technol. 114 (2022) 81–89, https://doi.org/10.1016/j.jmst.2021.12.003.
[47] Y. Jiang, Z.Y. Peng, S. Zhang, F. Li, Z. Liu, J. Zhang, et al., Facile in-situ Solvothermal Method to synthesize double shell $ZnIn_2S_4$ nanosheets/TiO_2 hollow nanosphere with enhanced photocatalytic activities, Ceram. Int. 44 (2018) 6115–6126, https://doi.org/10.1016/j.ceramint.2017.12.244.
[48] H. Xu, Y. Jiang, X. Yang, F. Li, A. Li, Y. Liu, et al., Fabricating carbon quantum dots doped $ZnIn_2S_4$ nanoflower composites with broad spectrum and enhanced photocatalytic Tetracycline hydrochloride degradation, Mater. Res. Bull. 97 (2018) 158–168, https://doi.org/10.1016/j.materresbull.2017.09.004.
[49] X. Pan, C. Shang, Z. Chen, M. Jin, Y. Zhang, Z. Zhang, et al., Enhanced photocatalytic H_2 evolution over $ZnIn_2S_4$ flower-like microspheres doped with black phosphorus quantum dots, Nanomaterials (2019) 9, https://doi.org/10.3390/nano9091266.
[50] J. Wang, D. Wang, X. Zhang, C. Zhao, M. Zhang, Z. Zhang, et al., An anti-symmetric dual (ASD) Z-scheme photocatalytic system: ($ZnIn_2S_4/Er^{3+}$:$Y_3Al_5O_{12}$@$ZnTiO_3$/ $CaIn_2S_4$) for organic pollutants degradation with simultaneous hydrogen evolution, Int. J. Hydrogen Energy 44 (2019) 6592–6607, https://doi.org/10.1016/j.ijhydene.2019.01.214.
[51] J. Zhao, X. Yan, N. Zhao, X. Li, B. Lu, X. Zhang, et al., Cocatalyst designing: a binary noble-metal-free cocatalyst system consisting of $ZnIn_2S_4$ and $In(OH)_3$ for efficient visible-light photocatalytic water splitting†, RSC Adv. 8 (2018) 4979–4986, https://doi.org/10.1039/c7ra12586k.
[52] Q. Gu, J. Long, H. Zhuang, C. Zhang, Y. Zhou, X. Wang, Ternary Pt/SnO_x/TiO2 photocatalysts for hydrogen production: consequence of Pt sites for synergy of dual co-catalysts, Phys. Chem. Chem. Phys. 16 (2014) 12521–12534, https://doi.org/10.1039/c4cp01496k.
[53] W. Chen, R.Q. Yan, J.Q. Zhu, G.B. Huang, Z. Chen, Highly efficient visible-light-driven photocatalytic hydrogen evolution by all-solid-state Z-scheme CdS/QDs/ $ZnIn_2S_4$ architectures with MoS_2 quantum dots as solid-state electron mediator, Appl. Surf. Sci. 504 (2020), 144406, https://doi.org/10.1016/j.apsusc.2019.144406.
[54] Y. Honda, M. Watanabe, H. Hagiwara, S. Ida, T. Ishihara, Inorganic/whole-cell biohybrid photocatalyst for highly efficient hydrogen production from water, Appl. Catal. B Environ. 210 (2017) 400–406, https://doi.org/10.1016/j.apcatb.2017.04.015.
[55] C.A. Caputo, L. Wang, R. Beranek, E. Reisner, Carbon nitride-TiO_2 hybrid modified with hydrogenase for visible light driven hydrogen production, Chem. Sci. 6 (2015) 5690–5694, https://doi.org/10.1039/c5sc02017d.
[56] S. Krishnamurthy, I.V. Lightcap, P.V. Kamat, Electron transfer between methyl viologen radicals and graphene oxide: Reduction, electron storage and discharge, J. Photochem. Photobiol. A Chem. 221 (2011) 214–219, https://doi.org/10.1016/j.jphotochem.2011.02.024.
[57] C. Kong, L. Qin, J. Liu, X. Zhong, L. Zhu, Y.T. Long, Determination of dissolved oxygen based on photoinduced electron transfer from quantum dots to methyl viologen, Anal. Methods 2 (2010) 1056–1062, https://doi.org/10.1039/c0ay00201a.
[58] H. Lu, R. Hu, H. Bai, H. Chen, F. Lv, L. Liu, et al., Efficient conjugated polymer-methyl viologen electron transfer system for controlled photo-driven hydrogen evolution, ACS Appl. Mater. Interfaces 9 (2017) 10355–10359, https://doi.org/10.1021/acsami.7b00069.
[59] A. Iagatti, L. Tarpani, E. Fiacchi, L. Bussotti, L. Latterini, P. Foggi, Charge transfer dynamics between MPA capped CdTe quantum dots and methyl viologen, J. Photochem. Photobiol. A Chem. 346 (2017) 382–389, https://doi.org/10.1016/j.jphotochem.2017.06.022.
[60] M.D. Peterson, S.C. Jensen, D.J. Weinberg, E.A. Weiss, Mechanisms for adsorption of methyl viologen on cds quantum dots, ACS Nano 8 (2014) 2826–2837, https://doi.org/10.1021/nn406651a.
[61] F. Gao, Y. Zhao, L. Zhang, B. Wang, Y. Wang, X. Huang, et al., Well dispersed MoC quantum dots in ultrathin carbon films as efficient co-catalysts for photocatalytic H_2 evolution, J. Mater. Chem. A 6 (2018) 18979–18986, https://doi.org/10.1039/c8ta06029k.
[62] B. Mei, K. Han, G. Mul, Driving surface redox reactions in heterogeneous photocatalysis: the active state of illuminated semiconductor-supported nanoparticles during overall water-splitting, ACS Catal. 8 (2018) 9154–9164, https://doi.org/10.1021/acscatal.8b02215.
[63] K. Wenderich, G. Mul, Methods, mechanism, and applications of photodeposition in photocatalysis: a review, Chem. Rev. 116 (2016) 14587–14619, https://doi.org/10.1021/acs.chemrev.6b00327.
[64] V. Naumkin A, Kraut-Vass A.W., Gaarenstroom S.J. Powell C. NIST X-ray Photoelectron Spectroscopy Database, NIST Standard Reference Database 20, Version 4.1. Natl Inst Stand Technol 2012. ⟨https://doi.org/10.18434/T4T88K⟩.

[65] L. Zeng, J. Luo, G. Mao, D. Wu, R. Li, L. Huang, et al., Boosted hydrogen evolution in alkaline media enabled by a facile oxidation-involving surface modification, Electro Acta 398 (2021), 139337, https://doi.org/10.1016/j.electacta.2021.139337.
[66] C. Li, P. Hu, H. Meng, Z. Jiang, Role of sulfites in the water splitting reaction, J. Solut. Chem. 45 (2016) 67–80, https://doi.org/10.1007/s10953-015-0422-1.
[67] Q. Li, Z. Chen, X. Zheng, Z. Jin, Study of photoreduction of $PtCl_6^{2-}$ on CdS, J. Phys. Chem. 96 (1992) 5959–5962, https://doi.org/10.1021/j100193a057.
[68] Y. Wang, Y. Wang, R. Xu, Photochemical deposition of Pt on CdS for H_2 evolution from water: Markedly enhanced activity by controlling Pt reduction environment, J. Phys. Chem. C 117 (2013) 783–790, https://doi.org/10.1021/jp309603c.
[69] Z. Shen, G. Chen, Y. Yu, Q. Wang, C. Zhou, L. Hao, et al., Sonochemistry synthesis of nanocrystals embedded in a MoO_3-CdS core-shell photocatalyst with enhanced hydrogen production and photodegradation, J. Mater. Chem. 22 (2012) 19646–19651, https://doi.org/10.1039/c2jm33432a.
[70] J.G. Yu, H.G. Yu, B. Cheng, X.J. Zhao, J.C. Yu, W.K. Ho, The effect of calcination temperature on the surface microstructure and photocatalytic activity of TiO_2 thin films prepared by liquid phase deposition, J. Phys. Chem. B 107 (2003) 13871–13879, https://doi.org/10.1021/jp036158y.
[71] F.B. Li, X.Z. Li, Photocatalytic properties of gold/gold ion-modified titanium dioxide for wastewater treatment, Appl. Catal. A Gen. 228 (2002) 15–27, https://doi.org/10.1016/S0926-860X(01)00953-X.
[72] M. Guo, Z. Xing, T. Zhao, Z. Li, S. Yang, W. Zhou, WS_2 quantum dots/MoS_2@WO_{3-x} core-shell hierarchical dual Z-scheme tandem heterojunctions with wide-spectrum response and enhanced photocatalytic performance, Appl. Catal. B Environ. 257 (2019), 117913, https://doi.org/10.1016/j.apcatb.2019.117913.